Influence of build angles on thin-wall geometry and surface texture in laser powder directed energy deposition

Gradl, P.R.; Cervone, A.; Colonna, Piero

DOI
10.1016/j.matdes.2023.112352

Publication date
2023

Document Version
Final published version

Published in
Journal of Materials Research and Technology

Materials & Design 234 (2023) 112352

Contents lists available at ScienceDirect

Materials & Design

journal homepage: www.elsevier.com/locate/matdes

Influence of build angles on thin-wall geometry and surface texture in laser powder directed energy deposition

Paul Gradl [a,*], Angelo Cervone [b], Piero Colonna [c]

[a] Propulsion Department, NASA Marshall Space Flight Center, Huntsville, AL, United States
[b] Space Systems Engineering, Delft University of Technology, Delft, Netherlands
[c] Propulsion and Power, Delft University of Technology, Delft, Netherlands

A B S T R A C T

Metal additive manufacturing (AM) is being used for mission-critical applications in both developmental and production components, driven by economic and technical benefits. Laser powder directed energy deposition (LP-DED) allows manufacturing of thin wall geometric features for various components at diameters larger than 2 m. The characterization of geometric capabilities and limitations is critical for establishing guidelines for end users of the technology. Within this study, several samples of enclosed vertical tracks were fabricated and characterized using LP-DED, with 1 mm-thick walls and varying inclination angles up to 45° using the NASA HR-1 alloy (Fe-Ni-Cr). The wall thickness, melt pool, and surface texture, inclusive of waviness and roughness, were evaluated and results presented. The experimental results indicate that the wall thickness increases exponentially above 30°. The surface texture was shown to be dependent on 1) excess powder adherence, 2) melt pool irregularities causing material droop, and 3) excess material. The experiment revealed that the mean roughness reduces with increasing wall angle for the downskin surface. The upskin roughness reaches a maximum peak at 20° and slowly reduces as powder adheres within the valleys. Both the downskin and upskin surface textures are dominated by irregular waviness generated by the melt pool.

1. Introduction

Additive manufacturing (AM) is gaining recognition as a viable manufacturing solution across multiple industries, transitioning from a mere prototyping tool to encompass the production of end-use parts and systems. The key advantages of AM distinguishing it from conventional manufacturing methods include cost reduction, complex part production, reduced schedules, and consolidation of components. Another advantage is the ability to create complex features unattainable through traditional or emerging manufacturing techniques, even when employing novel metal alloys. Metal AM encompasses a myriad of processes, with unique benefits and disadvantages affecting different build sizes, microstructure based on various melting or solid-state bonding methods, and geometry ranging from coarse to finely detailed features. These high-level process categories include:

- powder bed fusion (PBF),
- directed energy deposition (DED), and
- solid-state (cold spray, ultrasonic additive manufacturing, additive friction stir deposition, and binder jetting) [1].

These metal AM processes are being developed and actively used in aerospace, medical, and industrial applications [2]. As each AM process evolves, it becomes imperative to comprehensively characterize the achievable geometries, microstructure, resulting properties, and processing economics associated with each specific technology and the corresponding metal alloys. Design for additive manufacturing (DfAM) guidelines are unique for each AM process and cannot be applied broadly from one process to another. Without a proper understanding of these guidelines, an end-use AM component may not meet the intended structural, thermal, dynamic, fluid flow, or life requirements. Most AM research on PBF and DED processes focuses on microstructure and related mechanical and thermophysical properties. There is limited research on the DfAM process as it relates to geometry capabilities and limitations [3–6].

Laser Powder Bed Fusion (L-PBF) is one of the most widely used AM processes, providing the ability to fabricate highly intricate details with internal features and resolutions with dimensions of 0.25 mm or finer [7–9]. The inherent complexity of L-PBF makes it an ideal manufacturing process for production of heat exchangers used in aerospace, power plants, electronics cooling, chemical processing, energy storage and conversion systems, and oil and gas applications [10]. L-PBF has reached a state of maturity and is actively employed in commercial and military aviation and spaceflight applications. It is utilizeded extensively for components such as liquid rocket engine heat exchangers

* Corresponding author.
E-mail address: paul.r.gradl@nasa.gov (P. Gradl).

https://doi.org/10.1016/j.matdes.2023.112352
Received 19 June 2023; Received in revised form 14 September 2023; Accepted 21 September 2023
Available online 22 September 2023

Terminology

α	angle of wall in degrees
AM	Additive manufacturing
BD	Build direction
DED	directed energy deposition
DfAM	Design for additive manufacturing
F	powder feedrate, in grams/min
K'	Proportionality constant (2.35)
λc	large-scale band pass filter (also Lc)
λs	small-scale (noise) filter (also Ls)
L-PBF	Laser powder bed fusion
LP-DED	laser powder directed energy deposition
n	Exponent (0.005)
NASA HR-1	Fe-Ni-Cr alloy for hydrogen resistant applications
P	Power, in watts
PBF	powder bed fusion
PSD	particle size distribution
Ra	Arithmetic mean directional roughness
Rz	Average directional maximum profile height
Sa	Average texture
Sdr	Developed interfacial area ratio
SEM	Scanning Electron Microscope
Sk	Core roughness
Sku	Kurtosis
Sp	Maximum peak height
Sq	Root mean square (RMS) height
Ssk	Skewness
Sv	Maximum valley depth
Sz	Maximum surface height
V	Traverse scan speed of deposition head, in mm/min
Wa	Arithmetic mean directional waviness
Wt	Wall thickness, in mm

(combustion chambers, nozzles), and parts incorporating integral cooling channels [11,12]. While L-PBF is common for components such as heat exchangers, it is limited in terms of achievable overall build volume. L-PBF components can be commonly built up to 400 × 400 × 400 mm with some machines capable of handling parts of up to 1 m diameter and height [1]. For parts that are beyond this size, directed energy deposition (DED) is an alternative [1,13]. Several review papers have been published on additively manufactured heat exchangers with an emphasis on L-PBF, but none mention the use of DED for thin-wall heat exchangers [14–18].

Laser Powder DED (LP-DED) can overcome the L-PBF size limitation while incorporating thin-wall (1 mm) internal channels. LP-DED (Fig. 1) uses a laser as the energy source and powder feedstock is blown into a melt pool to deposit beads [19]. The blown powder deposition head and the laser beam optics are mounted on a gantry (or robot) to allow for the precise motion control needed to manufacture thin-wall features [20]. Freeform structures are fabricated based on toolpaths generated from CAD models. The process allows for internal features such as channels and flow passages to be produced [21,22]. Examples of LP-DED applications include casting and forging replacements, cladding and repair, fabrication of primary structures, as well as thin-wall large diameter structures such as heat exchangers with integral channels [13,23].

Research has been conducted to explore the feasibility of creating vertical single-bead thin-walls (<1.5 mm) using the LP-DED process, but focused on materials characterization and mechanical testing of vertical or horizontal surfaces [24–33]. A gap in prior LP-DED studies is the characterization of thin-wall geometric limitations including build angles, features (holes, channels, slots, etc), thickness variation, surface texture, and the combination of these attributes [13,34–36]. These features, including thin-walls and internal flow passages, are common in complex AM parts, particularly in applications such as aerospace or industrial heat exchangers. Thin-wall feature characterization is particularly important due to decreased powder efficiency in the process, which can impact the geometry [37]. The understanding of the DfAM guidelines for thin-wall LP-DED bridge the divide between fundamental research and practical implementation [20].

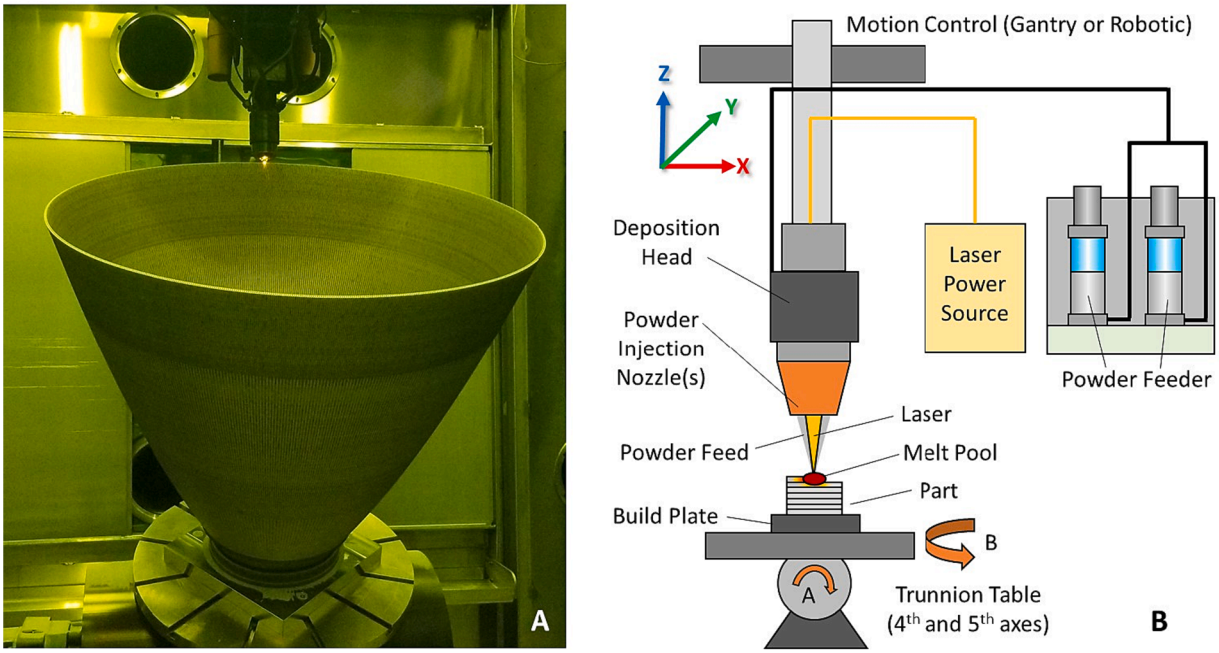

Fig. 1. Laser Powder DED System. A) Large scale integral channel part (>1 m) during fabrication, B) Overview of the LP-DED system components [11].

A few studies explored LP-DED of thin angled walls limited to stainless steel (SS) alloys. Kalami and Urbanic conducted LP-DED experiments to produce a SS 410 dome structure with 2 mm walls, which focused on developing an algorithm for process planning multi-axis toolpaths and collision avoidance of the deposition head and the part [38]. The research was expanded to study directional surface roughness (Ra) and concluded that the interfaces between toolpath partitions caused significant changes in roughness [39]. As a result of utilizing partitioned toolpaths and maintaining the deposition head in a normal position, no definitive conclusions could be drawn regarding the impact of changing angles on surface roughness. Kaj et al. studied 2 mm walls deposited with LP-DED SS 316L and focused on 5-axis motion control [40]. The research indicated a 32.5° wall was achievable with LP-DED but did not provide any corresponding surface texture or roughness data. Wang et al. deposited 1 mm thick angled walls up to 32.9° using SS 17-4PH with collapses occurring above that angle [41]. The research concluded that lowering the layer height (Z–increment) to 0.43 mm resulted in more consistent angles (+/-0.9°), but also collapsed above 31°; no data on the surface texture was included.

Surface texture is another key geometric attribute for design since it can impact mechanical properties such as fatigue life, and, in case of internal fluid flows, heat transfer, and friction factors [42]. It is well known that the surface texture for AM produced parts is higher compared to traditional manufacturing techniques [43,44]. Proper filtering of measurements is of paramount importance when analyzing surface texture, encompassing form, waviness, and roughness. When defining the surface (i.e. roughness) as an input for fluid flow analysis, relying solely on roughness data may not provide an accurate representation of the complete surface profile. [45,46]. The combination of height, spatial, hybrid, and functional parameters within comprehensive parameter groups enables a holistic understanding of the surface properties. [47]. Each of these texture parameters aid in describing results from manufacturing processes or end-use function (i.e. wear, lubrication, friction, fatigue, sealing, etc) [47]. Surface texture measurement is important during manufacturing to validate design assumptions and reduce uncertainty. It is also critical to measure and characterize surfaces throughout manufacturing operations. These experimental data are used to discern the underlying mechanisms behind the observed texture, such as waviness and roughness. This helps guide the total amount of material that needs to be removed during subsequent polishing or machining operations if a certain texture is required.

Surface texture is a direct outcome of the AM build process and is influenced by various factors, including the build orientation, wall angles, feedstock, process parameters, wall thickness, and the material being used [48]. It is known for L-PBF that surface texture varies significantly based on the angle and orientation (upskin or downskin) of a surface [49,50]. It has been shown that increasing the angle of downskin surfaces, relative to the build direction, increases the surface roughness due partially to unmelted powder adherence and dross formation [51,52]. Dross is excess material from overheating that forms at surface as the laser melts the powder and the material subsequently cools [53,54]. These studies all focused on evaluating the upskin and downskin surface texture related to L-PBF, but a gap exists related to this characterization for LP-DED.

Prior studies about L-PBF and LP-DED indicated that the observed stair step (or stair case) effect increases the surface roughness [32,55,56]. The stair stepping is the result of slicing the part into defined layers. The part is built in these layers with a determined height increase (Z-orientation step up) of the deposition head that is programmed. The step is a resultant of these layers, which can be more pronounced as the surface angle increases relative to the build direction [57,58]. While the literature addresses the impact of the stair step as a form of roughness, it often does not segregate the data to distinguish waviness, creating a gap with respect to the full characterization of the LP-DED process.

This paper summarizes research that used a variety of experimental data to characterize the geometry dependency of various samples fabricated using LP-DED. The study focuses on 1 mm wall thickness samples fabricated at angles up to 45° using hydrogen-resistant NASA HR-1 (Fe-Ni-Cr) alloy. These samples were deposited as freeform "racetracks", with a straight wall on each side and 180 bends. The purpose of this experiment was to characterize deposition angle dependency for build limitations, upskin and downskin surface texture, wall thickness, and general microstructure. An equation was developed to predict wall thickness. These results are intended to advance the understanding of DfAM for the LP-DED process and to establish attributes for design and research engineers. The experimental results obtained are specifically applicable to the NASA HR-1 alloy. However, it is worth noting that the observed trends may have broader applicability to other alloys, provided that additional data collection is conducted.

2. Methodology

2.1. DED system and samples

Ten NASA HR-1 alloy samples at angles varying every five degrees were deposited on an RPM Innovations (RPMI) 557 LP-DED machine with an argon-inert build chamber. The 557 system incorporated an infrared (IR) continuous wave gaussian profile 3 kW IPG laser, three coaxial nozzle within the deposition head, 5-axis motion control, and disc powder feeder with agitation capabilities. The motion control system was a Cartesian gantry-type system with a tilt and rotate trunnion table, although the trunnion table was not used in this experiment. The samples were built using a 2 +1 axis approach, meaning each layer was deposited and the deposition head translated in height by +0.254 mm to deposit the next layer. The deposition head remained perpendicular to the build plate for all samples.

The samples were deposited as an enclosed racetrack (straight walls and 180° radii) to provide for dimensional stability. The baseline sample was built vertically, with the identifier referencing the build direction (0°); subsequent samples are identified in reference to the angle offset from the vertical build direction (5°, 10°, …45°). The baseline 0° sample geometry was identical to a prior study in which deposition parameters were varied using the same NASA HR-1 alloy [59]. While the use of 5-axis systems is possible, it is not feasible for every part and the practical application of complex LP-DED parts still uses a 2 +1 (layer-wise slicing) and a combination of multi-axis toolpath planning. The samples were single-width passes (1 mm) at 76 mm length (Y-direction), 25 mm height (Z-direction), and 25 mm span between the adjacent wall (X-direction). The samples were built on an A36 mild steel 12 mm thick base plate. The layers for each sample were built individually, but simultaneously to allow for proper cooling between passes. All samples were evaluated in the as-built condition with no stress relief or other heat treatments and no surface cleaning or post-processing. The samples were removed from the build plate using a bandsaw and deburred on the bottom edge only. The samples from each angle are shown in Fig. 2.

The upskin is referred to as the surface angled upward relative to the deposition head. This is also the outer surface on all samples. The downskin is the downward facing and the inner surface. The upskin and downskin terminology is consistent with previous L-PBF research [4].

The samples were built successfully up to 30° (Fig. 2). The 35° and 40° specimens featured discontinuities in the radius. The 45° specimen had discontinuities in the radius and failed in the opposing wall. Once the deposition had challenges in a layer, this discontinuity would propagate and become worse with increased height. The straight wall that was successfully built served as the basis for all characterization and analysis.

2.2. Deposition parameters

The deposition parameters used for the experiment are listed in Table 1. The optimal parameters were selected based on a prior design of experiments to optimize high density microstructure and reduced build

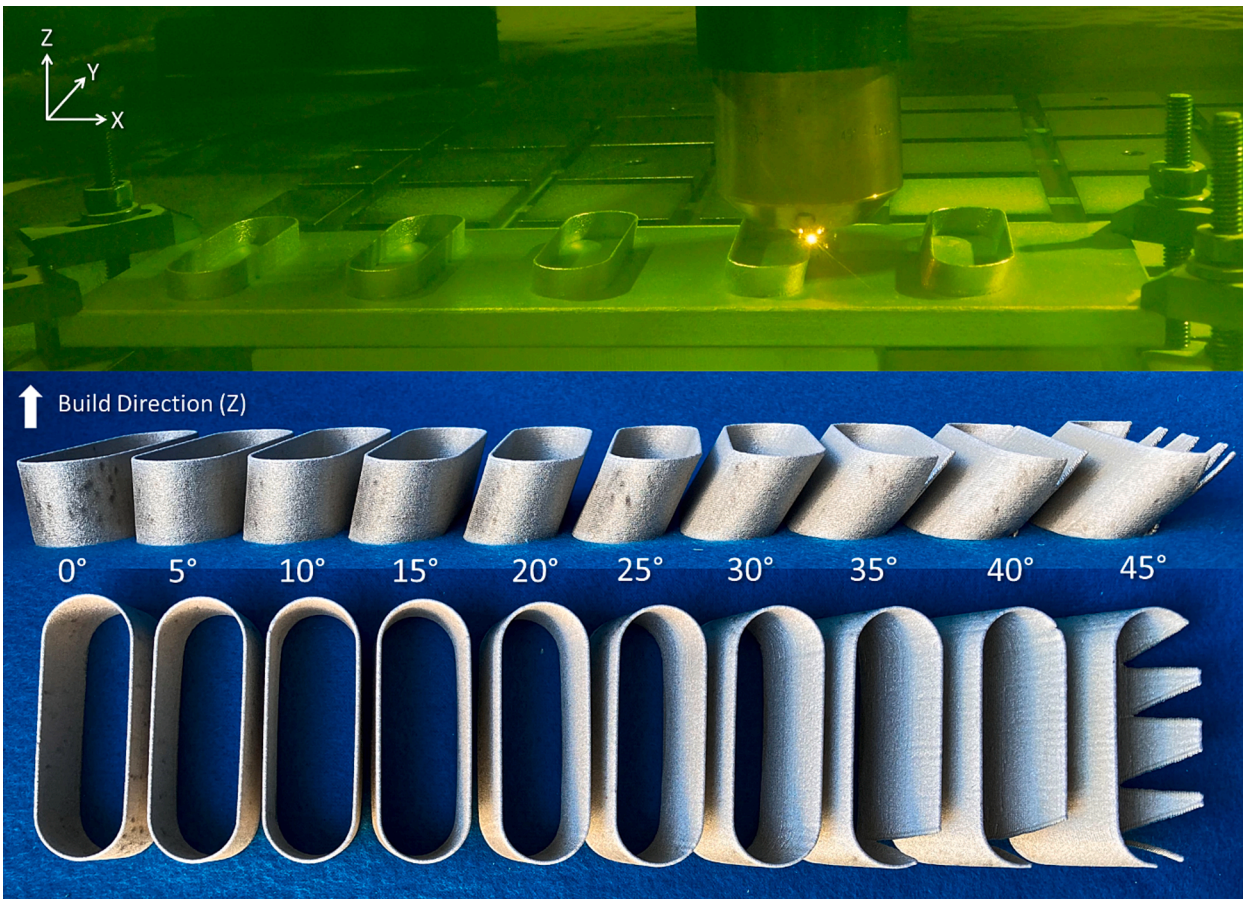

Fig. 2. As-built NASA HR-1 alloy angled specimens removed from the build plate.

Table 1
Parameters used for angled racetrack sample deposition.

Power (W)	Powder Feed rate (grams/min)	Travel Speed (mm/min)	Layer Height (mm)
350	23	762	0.254

time [23,59,60]. Argon was used as the powder feedstock carrier and shielding gas. The deposition head was fixed normal to the surface and the standoff distance was actively monitored and controlled. The layer height remained constant at 0.254 mm and X-axis translation adjusted based on the angle of the sample. The start and stop points were randomized for each sample. The trunnion table was locked and not used for these samples. While acknowledging that the use of a trunnion table could potentially increase the maximum build angle, it is important to note that this build approach for thin-wall complex hardware designs may not always be feasible and is not the primary focus of this study.

2.3. NASA HR-1 alloy

NASA HR-1 is a Fe-Ni-Cr superalloy used in high pressure hydrogen components, such as heat exchangers. It was developed for resistance to hydrogen environment embrittlement (HEE). NASA HR-1 provides high strength and high ductility in harsh hydrogen environments such as liquid rocket engine nozzles and heat exchangers and it is derived from the A-286 and JBK-75 alloys [61,62]. The powder was rotary atomized by Homogenized Metals Inc. (HMI), with a particle size distribution (PSD) of 55–105 μm meeting +140 mesh at 0 % and −325 mesh at 3.2 % per ASTM B214 using a Microtrac (Ver 11.1.0.6), and chemical composition provided in Table 2 (HMI powder lot HRA7). A SEM image of the morphology is shown in Fig. 3. The Oxygen content was 59 ppm and Nitrogen content was 9 ppm. The chemistry was measured using Inductively Coupled Plasma (ICP) at HMI. The peak powder size was 69 μm and a Vega3 Tescan Scanning Electron Microscope (SEM) using Backscatter Electron (BSE) showed mostly spherical particles with a few satellites and random distribution of occasional oblong particles. The powder cumulative distribution has 10 % of particle sized below 58 μm (D10), 90 % below 85 μm (D90), and 99 % below 105 μm (D99) with a median particle size of 69 μm. Virgin powder was used for all builds. The samples were evaluated in the non-heat treated (as-built) condition.

2.4. Surface metrology and imaging

Surface texture measurements were obtained using a non-contact Keyence VR-5200 pattern light projection optical profilometer. The setup included three telecentric lenses with 80x magnification capability and an overlap of 20 %. Each sample was measured on the upskin (outer) surface and then sectioned inside of the radii to allow access to the inner

Table 2
Chemical composition of NASA HR-1 alloy powder (HMI Lot HRA7).

	Fe	Ni	Cr	Co	Mo	Ti	Al	V	W
Wt. %	Bal.	34.03	14.64	3.75	1.84	2.46	0.23	0.3	1.59

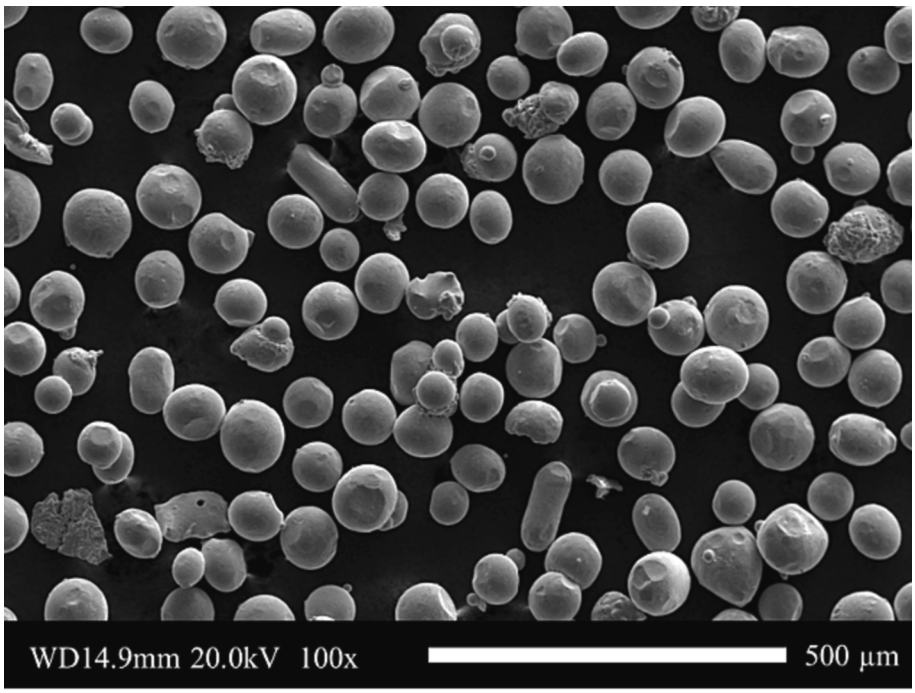

Fig. 3. SEM image of NASA HR-1 (55–105 µm) powder morphology.

surface. The downskin (inner) surface was then measured. The surface scanning covered a total area of 43 mm by 16 mm shown in Fig. 4. Areal surface measurements were reported in addition to directional legacy measurements. The texture measurements are reported along with a brief explanation and mathematical definition [46,47,63] in Table 3.

All areal surface measurements are reported according to ISO 25178–2:2021 [63,66]. A surface form correction was applied to remove any tilt and curvature from any residual stress distortion of the samples. The data around the edges of the measurement was eliminated using an end effect correction. A reference plane was then established. For the area surface measurements, the primary texture profile was unfiltered (denoted as primary) using form correction only. To extract roughness from the areal surface, a λc spatial frequency cut-off filter of 0.8 mm (i.e., a roughness filter) was applied per ISO 4288–1996. A λc of 2.5 mm was also evaluated but was too large. Measurement uncertainty was obtained by repeating measurements on a single sample five times to determine a 95 % confidence interval.

When analyzing texture measurements, it is important to consider the end use application to obtain appropriate results [39]. One potential application of the thin-wall LP-DED process is the fabrication of heat exchangers with integral channel fluid flow. These heat exchangers are built with the channels running in the vertical build direction (Z). Thus, the directional measurements are reported in the vertical build direction (Fig. 4). Five symmetrical vertical lines were placed on the sample image and measurements averaged to report the waviness and roughness. For the directional measurements, form correction was also applied along with λc of 0.8 mm and a λs of 2.5 µm to eliminate noise at a 300:1 ratio (λc/ λs) per ISO 4228–1996. This allowed for the segmentation of directional waviness (Wa) and roughness (Ra) effects. Directional measurements are reported according to ASME B46.1 [65].

The surface samples were imaged using a Hitachi S3000H SEM on the upskin and downskin. Each sample was then sectioned along the

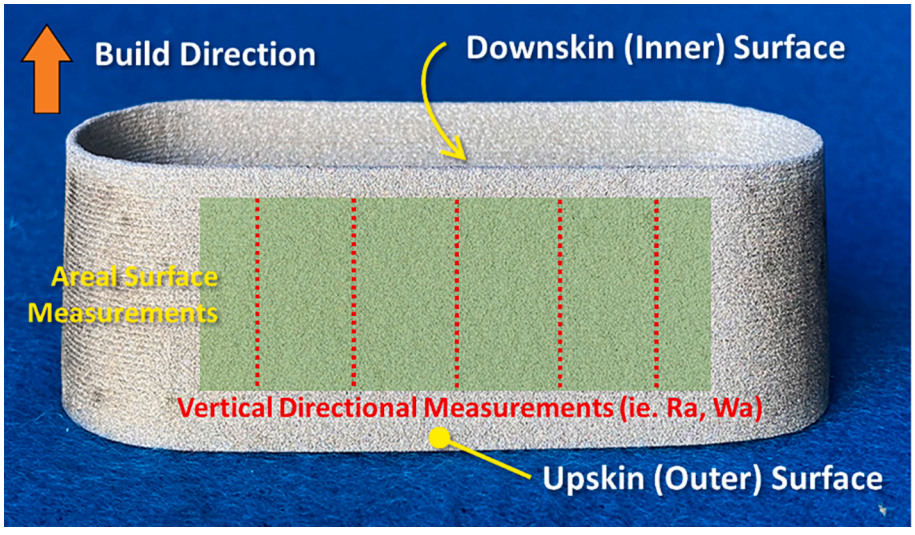

Fig. 4. Terminology for sample measurement (example of 20° wall sample).

Table 3
Description of surface parameters and definition.

Description of Surface Parameter	Mathematical Definition
Average texture (Sa) – average areal roughness across the entire 3D surface relative to a best fit plane.	$Sa = \frac{1}{A}\iint_A \lvert Z(x,y)\rvert dxdy$
Root mean square (RMS) height (Sq) –standard deviation of the height distribution.	$Sq = \sqrt{\frac{1}{A}\iint_A \left\lvert (Z(x,y))^2 \right\rvert dxdy}$
Maximum peak height (Sp) – absolute highest single points found on the 3D surface, filtered to eliminate erroneous peaks.	$Sp = \max(Z(x,y))$
Maximum valley depth (Sv) – absolute lowest single points found on the 3D surface, filtered to eliminate erroneous peaks.	$Sv = \lvert \min(Z(x,y)) \rvert$
Maximum surface height (Sz) – defined as the total surface height based on the summation of the maximum peak height and valley depth	$Sz = Sp + Sv$
Skewness (Ssk) – Represents the asymmetry of the surface texture based on a nominal plane, where 0 is ideal, >0 is dominated by peaks, and < 0 is valleys.	$Ssk = \frac{1}{Sq^3}\left[\frac{1}{A}\iint_A (Z(x,y))^3 dxdy\right]$
Kurtosis (Sku) – Determines inordinately high peaks or valleys, where 3.0 is ideal, >3.0 is peaks, and < 3.0 is valleys.	$Sku = \frac{1}{Sq^4}\left[\frac{1}{A}\iint_A (Z(x,y))^4 dxdy\right]$
Developed interfacial area ratio (Sdr) – Percentage of the overall surface area that contributes to the texture amplitude and spacing compared to an ideal plane across the entire measured area.	$Sdr = \frac{1}{A}\left[\iint_A \left(\sqrt{\left[1 + \left(\frac{\partial z(x,y)}{\partial x}\right)^2 + \left(\frac{\partial z(x,y)}{\partial y}\right)^2\right]} - 1\right) dxdy\right]$
Core roughness (Sk) – defined as the distance between the highest and lowest levels of the core surface height, filtered to eliminate predominant peaks and valleys.	$Sk^* \approx Sz - Spk - Svk$
Arithmetic mean directional roughness (Ra) – average deviation from a mean line based on a direction such as parallel (vertical) to the build direction or perpendicular (horizontal). Data are filtered using < λc, which removes form and waviness of the surface.	$Ra = \frac{1}{Lx}\int_0^{Lx} \lvert Z(x)\rvert dx$
Average directional maximum profile height (Rz) – average height difference between highest peaks and lowest valleys (using 5 of each) along a sampling length in a defined direction (vertical build direction). Data are filtered using < λc, which removes form and waviness of the surface.	$Rz = \max(Z(x)) + \lvert min(Z(x)) \rvert$
Arithmetic mean directional waviness (Wa) – average height of widely spaced component of the overall profile along a direction such as parallel (vertical) to the build direction or perpendicular (horizontal). Data are filtered using < λc, which removes form and waviness of the surface.	$Wa = \frac{1}{Lx}\int_0^{Lx} \lvert Z(x)\rvert dx$

*Sk is approximated and detailed procedures to obtain can be found in [64] and [65].

center axis and mounted and polished according to ASTM E3 using a Presi automatic polisher. The samples were polished using 0.5 μm colloidal silica and optical images obtained. Samples were then etched using etchant #13 (10 % Oxalic Acid, Electrolytic) and optical imaging completed again. All optical images were obtained using a Keyence VHX digital microscope. Porosity, thickness, meltpool, and powder particle count measurements were analyzed using Image J (Version 1.53e). Eight thickness measurements were obtained normal to each wall (across) and averaged. The distance between each melt pool (height), perpendicular to wall thickness, was also measured for each wall and averaged. The low angle samples (<10°) included approximately 12 melt pool measurements and angles > 10° were measured with a minimum of eight melt pools. A 95 % confidence interval was calculated and reported for these measurements. Particle count was determined by examining the number of particles in two 1 mm^2 areas and averaging. This was obtained from the SEM image at 50x.

3. Results and discussion

The measurements were obtained in a sequential order per sample: texture, SEM, optical images. However, they are presented here per type of measurement with the aim of providing a comprehensive understanding of the surface texture and associated geometry.

3.1. SEM image analysis

SEM images are shown in Fig. 5. Visually, the adhered powder occurrences drastically reduce on the downskin with increasing angle. The opposite is observed with the upskin whereby more powder adheres to the surface. As the angle of incidence increases relative to the deposition nozzle, the powder can bond more directly to the trailing and edges of the melt pool for the upskin. The downskin surface is more protected as the angle increases. An illustration of the vertical and angled powder impingement in the samples is shown in Fig. 6. Despite the enclosed racetrack samples, particle impacts are still possible. This is evident from the observations of ricochets and the recirculation of powder, as previously put into evidence [59].

Based on the SEM images, the particle count (per mm^2) was determined at two locations on the surface and averaged. These data sets are shown in Table 4. The particle count analysis confirms the increase in adherence for the upskin and reduced powder for the downskin, although no inference should be made from this observation related to surface texture without proper filtering for roughness. The increase in angle facilitates a longer particle resonance time due to flow stagnation from the impingement of the deposition nozzle (Fig. 6). Additionally, the smaller diameter melt pool (<1 mm) decreases the powder capture efficiency, leaving approximately 80 % of the powder available to adhere to the surface of the solidified material [37,67]. A depiction of the smaller melt pool (1 mm) is shown in the supplemental materials. Due to gravity, the powder will move down the surface of the angled wall and bond to the melt pool as it is cooling as indicated by the increased particle count.

3.2. Optical image analysis

From optical images of the sectioned samples several sets of data were collected. The porosity was measured for each sample in the polished unetched condition (non-heat treated) with the highest porosity being 0.14 %, as shown in Table 4. This is consistent with prior results on vertical 1 mm thick NASA HR-1 specimens [59] and no trends are apparent based on the angle of the sample. Density was also obtained using the Archimedes method and is provided in the supplemental materials; there were no correlations observed on samples based on the wall angle. The wall thickness was measured for each sample normal to the wall and results provided in Table 4. Fig. 7 shows that, as the angle increases, there is a corresponding increase in the normal wall thickness. The wall thickness linearly increases by 7 % from 0° to 25° and then increases exponentially from 25° to 45°. The optical images indicate a transition from partially melted and adhered powder at lower angles to a more random surface profile as the angles increase, more so for the downskin surface (Fig. 8). The downskin surface at the high angles shows instances of subsurface unmelted powder. The partially melted and adhered powder is observed regularly on the upskin surface with more instances at the higher angles.

The increased wall thickness is due to the material droop on the downskin side and excess material deposited on the upskin side. The visualized melt pool can be observed in Fig. 7 along the centerline of the sample. The material droop is made evident by the color change of etched samples and below the nominal melt pool. The Marangoni forces move the material outwards in the melt pool and this material is solidified at the edges causing this chaotic texturing [68,69]. Unmelted subsurface powder is also observed below the chaotic texturing (Fig. 8). Above 30°, gravity has an impact, breaking the surface tension and causing the fluid metal to droop below the nominal melt pool and then solidify. This droop is distinctively different from the dross phenomenon in L-PBF [54] since the melt pool terminates prior to the downskin edge of the specimens. The excess material above the nominal melt pool increases due to the direct impingement of the powder and inert gas and causes the remelted and deposited material to flow upwards, in addition to outwards [70].

It was observed from the experimental dataset, that the wall thickness could be normalized when divided by the cosine (α) function, where α is the angle of the deposited wall. The adjusted wall thickness has been demonstrated to exhibit a high level of consistency, which is corroborated by the measured thickness data (Fig. 9). Based on the observation that the wall thickness can be adjusted with the angle, this concept was applied to predict the wall thickness based on deposition parameters. Mazzarisi et al. reviewed and evaluated multiple models to predict wall thickness for single-beads based on laser power (P) measured in watts (W), powder feed rate (F) measured in grams/min, and traverse scan speed (V) measured in mm/min [68]. The validation testing has demonstrated a reasonable correlation with the proposed models. Kalami et al. discuss the relationship between the build layer height and its variation based on the angle. However, they do not specifically explore the relationship between the build layer height and the resulting wall thickness. [38]. With the help of this dataset, these approaches were modified resulting in an equation to predict the wall thickness (Wt) measured in mm, which reads

$$Wt = \frac{\frac{P}{VF^n}K'}{\cos\propto} \tag{1}$$

where Wt = thickness in mm; n = Exponent (0.005); K' = Proportionality constant (2.35); and α = angle of wall in degrees. The exponent and constant were fitted using the experimental data. The model shows a good correlation with the measured thickness and peak error of 3.5 % for the current set of NASA HR-1 samples.

The melt pool can be distinguished in the etched optical images and

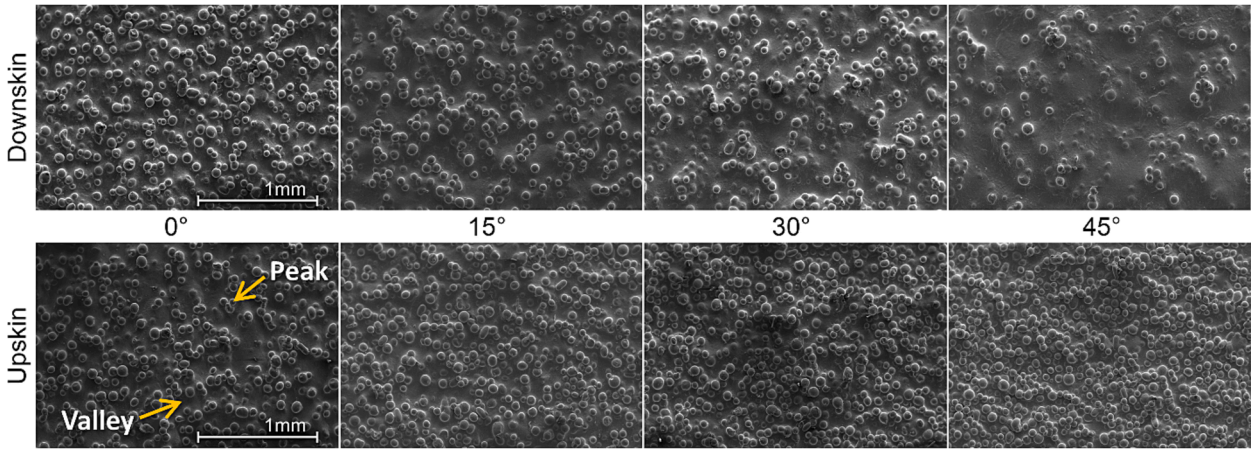

Fig. 5. SEM images of the normal surface for upskin and downskin surfaces (additional images provided in supplemental materials). Scale is the same for all images.

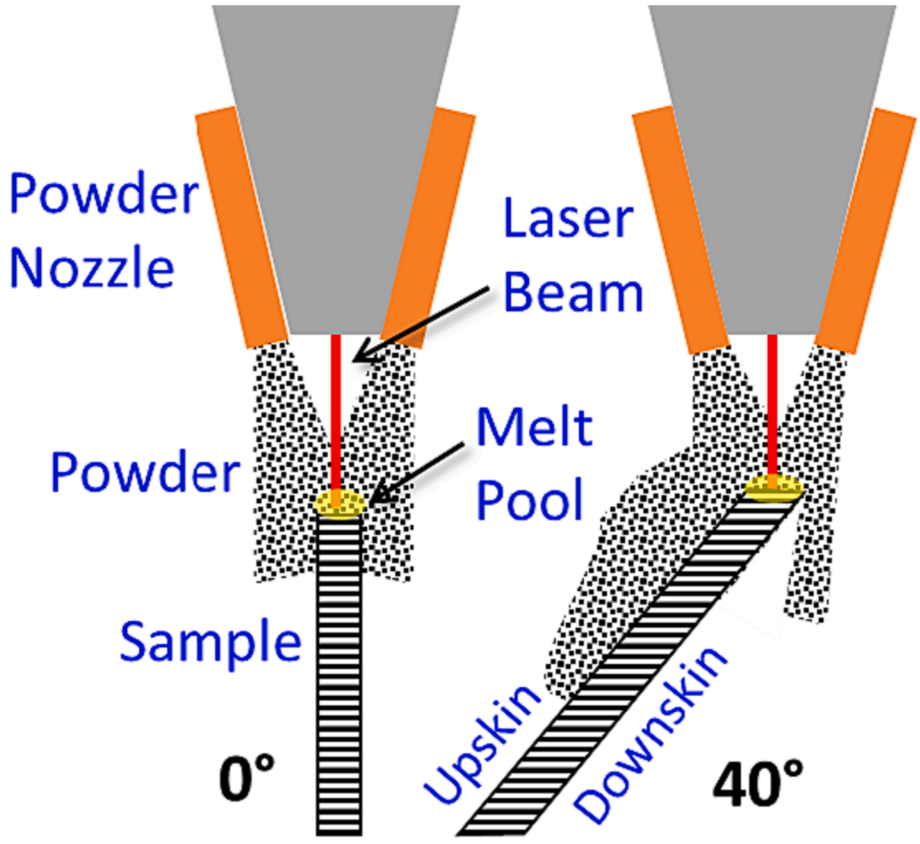

Fig. 6. Example of powder impingement for vertical and angled sample.

Table 4
Data from SEM and Optical Image Measurements.

Angle (°)	Particle Count, Downskin (Inner)	Particle Count, Upskin (Outer)	Normal Wall Thickness (μm)	Melt Pool Height (μm)	Optical Porosity (%)
0	96	93	1056 ± 24	253 ± 8	0.13
5	92	99	1046 ± 26	252 ± 17	0.11
10	92	120	1082 ± 17	259 ± 14	0.04
15	84	122	1079 ± 13	259 ± 10	0.07
20	80	126	1115 ± 15	269 ± 16	0.07
25	80	140	1132 ± 13	272 ± 10	0.10
30	68	142	1192 ± 14	287 ± 14	0.14
35	63	166	1306 ± 21	308 ± 13	0.05
40	54	179	1370 ± 15	336 ± 12	0.03
45	36	181	1535 ± 18	361 ± 18	0.05

was measured perpendicular to the wall and along the centerline. The vertical distance between the visible melt pools was obtained and averaged. Based on thickness of the sample at 0° and prior research of the NASA HR-1 melt pool with identical parameters [59], a size can be assumed and overlayed for each sample in Fig. 7. From this, the number of layers penetrated with subsequent deposition layers can be determined. An average of four deposited layers were subjected to remelting with each subsequent pass when the angle was less than 25°. When the angle exceeded 25°, three layers were remelted. The perpendicular melt pool height is shown in Fig. 10. The melt pool height was adjusted using the cosine function and shown in the graph. The measurements indicate that the height distance of the melt pool increases with the angle when measured vertically. However, the adjusted step over used to create the desired angle, along with the fixed Z-height of 0.254 mm, demonstrates highly repeatable motion control, a stable melt pool, and a satisfactory solidification process. The adjusted angle wall thickness (Fig. 9) also indicated a consistent melt pool. These findings establish the melt pool's robust stability, ruling out arbitrary material deposition related to height or thickness. The adjusted data sets confirm that the downskin droop and upskin excess material are not related to an unstable melt pool, but rather to gravity effects.

3.3. Surface texture characterization

3.3.1. Surface texture with primary filter

The initial areal surface texture was measured and evaluated using a form correction factor only. This allowed characterization of the full profile in terms of waviness and roughness. The Sa is shown in Fig. 11a: the inner and outer surfaces of the vertical wall (0°) feature a similar average surface texture. The average areal surface texture of the inner surface is slightly higher than the external surface consistent with prior measurements [59]. This is due to the enclosed racetrack walls allowing for powder rebounds and recirculation causing excess adherence. A minor change in the wall inclination of 5° results in a reduced amount of powder adhering to the downskin (inner surface) as it angles away from the deposition nozzle. The average texture of the outer surface (upskin) increases with the direct impact of the powder from the deposition nozzle. The upskin texture is driven by roughness from the powder but also by variations in the solidification of the melt pool, and it continues to increase linearly up to an angle of 35°, stays near level and then a slight drop occurs at 45°. The downskin texture shows no appreciable differences up to an angle of 30°, while for larger angles it increases exponentially. This indicates that particle adhesion alone cannot be used to determine texture and that other mechanisms cause this drastic change. The observed downskin texture varies with the angle and aligns with the thickness data and occurrence of material droop.

The maximum height of the surface (Sz) in Fig. 11b shows that the upskin surface texture decreases with increasing angles. Greater powder adherence is observed, but several particles have the capability to fill in

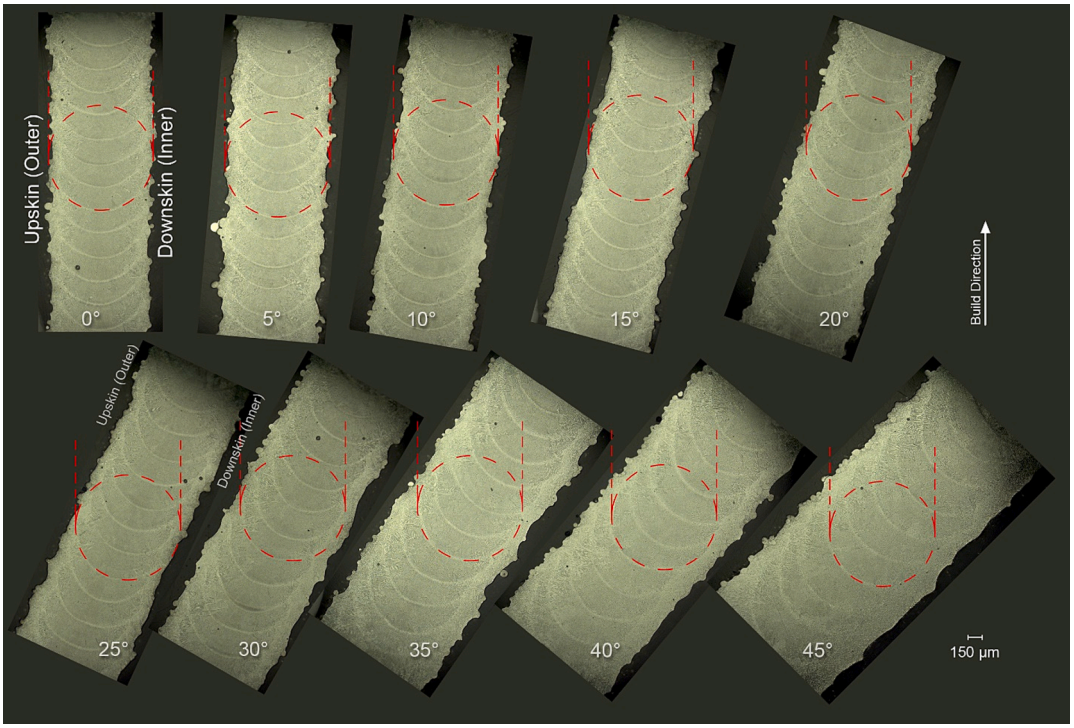

Fig. 7. Wall thickness and melt pool visualized on angled wall samples.

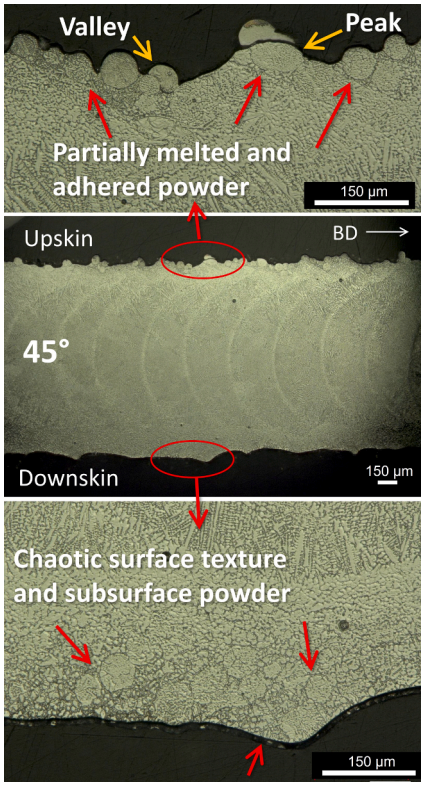

Fig. 8. Partially melted and adhered powder shown for the upskin surface and chaotic texturing and subsurface powder shown for the downskin of the 45° wall sample.

the valleys, thereby contributing to a decrease in the observed effect. This is corroborated by the observation that the maximum peak height (Sp) decreases, while the maximum valley depth (Sv) remains constant.

The downskin suggests a general increase of maximum height, where peaks dominate the surface texture. In order characterize this attribute, the skewness and kurtosis parameters were evaluated and are shown in Fig. 11c and Fig. 11d, respectively. The skewness (Fig. 11c) is plotted with the normal wall thickness to identify abnormalities related to symmetry. The plot therefore reveals that the upskin is symmetric about the plane, whereby peaks and valleys are randomly distributed. Up to an angle of 30°, the inner downskin surface is symmetric. Beyond this angle, a predominance of peaks becomes evident, which is coherent with the drastic changes observed in the wall thickness. The powder count analysis demonstrates that powder is less adherent in this case, therefore the asymmetrical peaks are governed by the droop of the material.

Fig. 11d allows to evaluate the kurtosis for excessively high peaks or valleys. A similar trend is observed in the Sz data of the upskin surface, which demonstrates a general decrease in the number of peaks as the angle increases. The downskin surface shows again a general increase of excessively high peaks with the increase in angle.

3.3.2. *Areal roughness and particle count*

The surface texture and filtered roughness are further examined in relation to the adherence of the powder to determine the factors contributing to the formation of the observed texture. Using no profile filter (i.e., primary), the texture of the upskin linearly increases with increasing particle count (Fig. 12a). This could indicate that powder adherence is dominant for the upskin roughness but cannot be determined conclusively without proper filtering. Fig. 12a also shows that the texture of the downskin surface initially decreases with reduced particle count. Starting at 30°, the surface texture linearly increases up to 40° and at 45° rises even more steeply. This indicates that the texture of the downskin surface is related to the powder adherence based on particle count.

The roughness filter, see section 2.4, was applied to the areal surface and plotted as a function of the particle count in Fig. 12b. The roughness (less than 0.8 mm wavelength) shows a clear trend for the downskin surface: the average roughness decreases with decreasing powder adherence, and this is also evident in the SEM images. The upskin surface exhibits a similar trend but only up to 20°. Beyond 20° the average

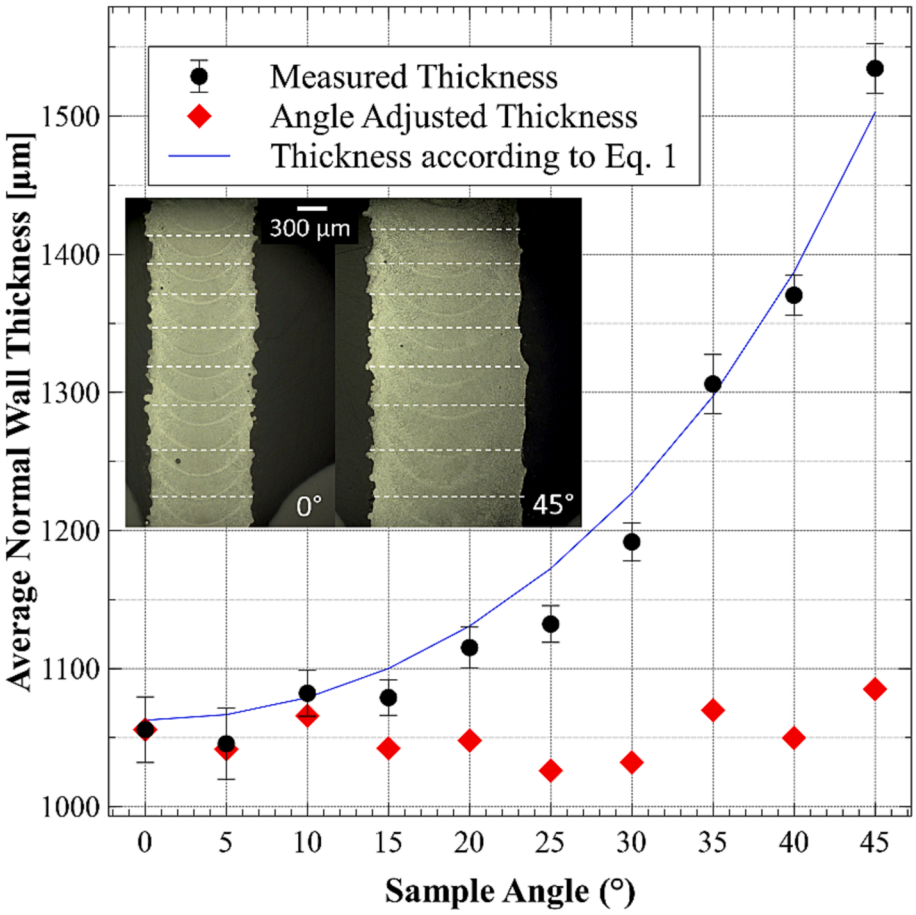

Fig. 9. Measured and adjusted wall thickness of the angled samples.

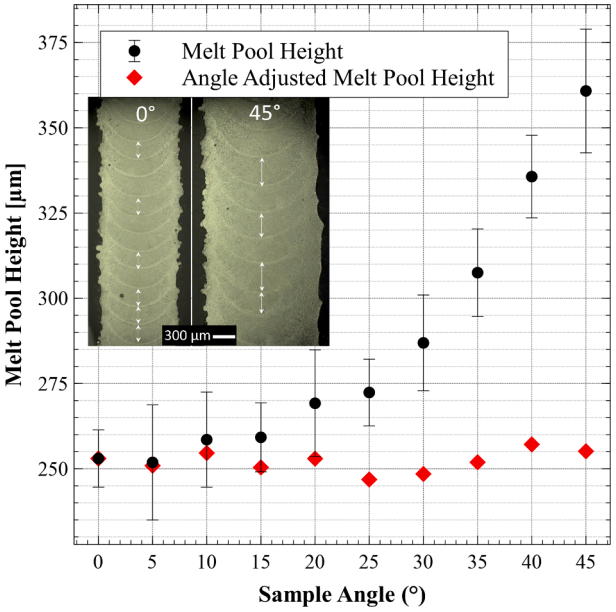

Fig. 10. Perpendicular melt pool height and adjusted height of the angled samples.

roughness is constant, and it is much lower at 45°. Above 20°, the particles continue to bond to the trailing edge of the melt pool as it cools but valley voids are filled. The optical images reveal that the texture extends to a depth of two powder particles, indicating that the excess particles are effectively filling in the valleys of the surface. The core roughness (Sk), whereby the predominant peaks and valleys were removed [64], was also evaluated, and its trend is identical to that of the Sa with the roughness filter. The Sk values ranges from 38 ± 0.2 µm to 51 ± 0.2 µm for the downskin surfaces and from 50 to 58 ± 0.2 um for the upskin surfaces. The filtered Sdr was also assessed, because it determines the overall contribution to the texture amplitude (shown in supplementary materials). The trends are identical to those obtained for the Sa and the Sk: the roughness is proportional to the particle count for the downskin surfaces and it reaches a maximum at 20° for the upskin surfaces.

This roughness comparison displayed in Fig. 12 put into evidence the significance of using appropriate filtering techniques. Significantly different conclusions could be drawn about the mechanism for the texture without properly evaluating all filtering options [71].

3.3.3. *Vertical directional roughness and waviness*

To better characterize roughness (Ra) and waviness (Wa) in the vertical build direction, the data set was filtered as discussed in section 2.4 and a comparison is shown in Fig. 13a. The directional average roughness for the upskin is higher than that of the downskin and driven by the direct particle impact with the melt pool. In contrast to the Sa values (Fig. 12), the upskin Ra does not indicate a reliance upon the angle and roughness values are similar at all angles. The upskin Wa does increase at angles above 30° due to chaotic disturbances in the melt pool creating the texture. It can be hypothesized that the increased melt pool disturbance can reduce the presence of partially assimilated surface particles [72]. This is observed in the maximum height roughness (Rz) in Fig. 13b, which is driven by the particle count above 25°, and also the waviness portion of the surface texture.

The downskin surface indicates similar directional roughness and

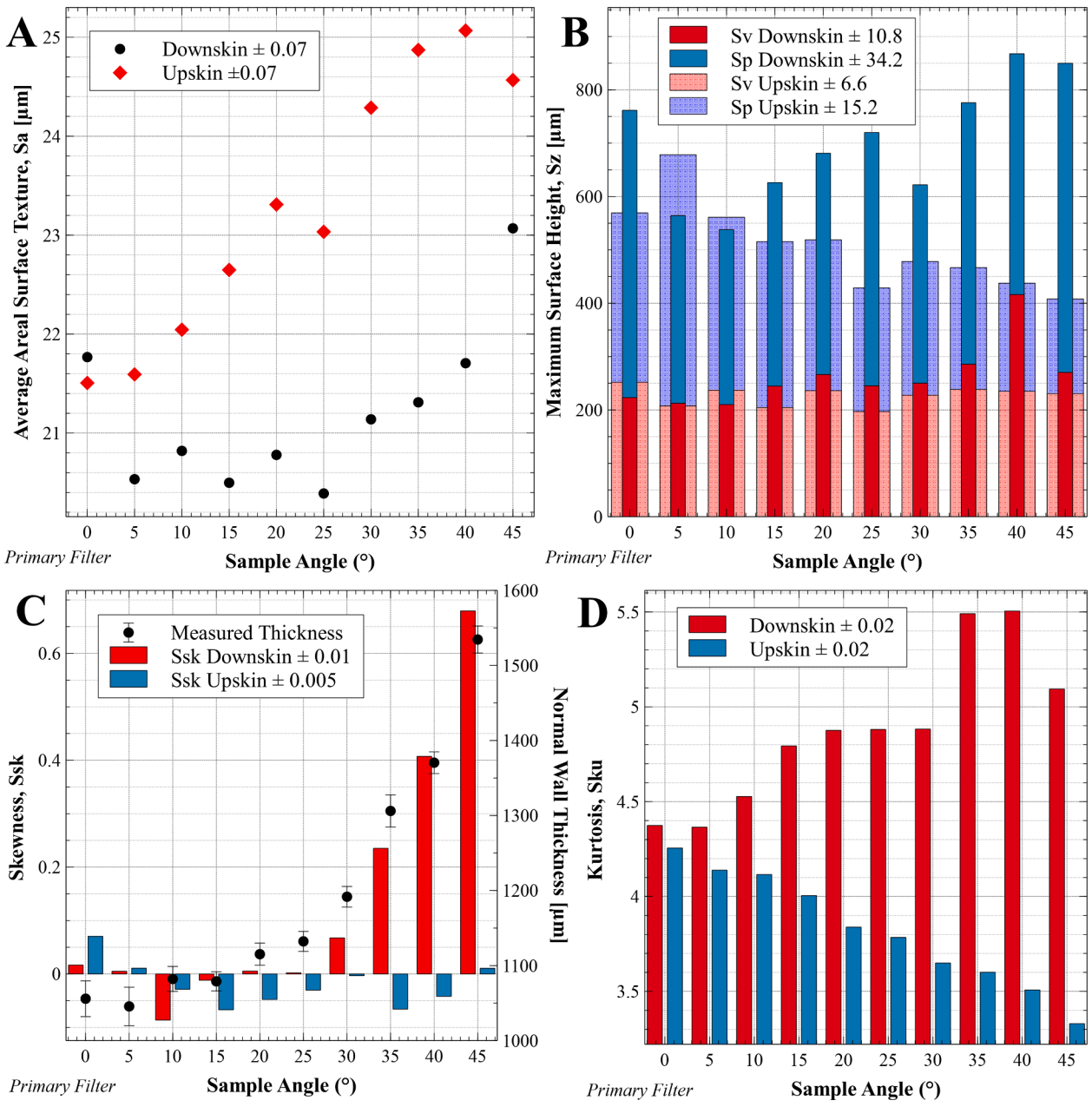

Fig. 11. Primary texture of areal surface: a) Sa, average surface texture; b) Sz, Sp, Sv, peak and valley height of surface; c) Ssk, skewness; and d) Sku, Kurtosis.

waviness at angles 0° to 30°. A linear increase in waviness and decrease of roughness is observed starting at 35°. Literature often suggests that the stair-stepping effect due to the build layers creates periodic waviness [35,73], but this is not observed in these samples with a layer thickness of 254 µm. The waviness is driven by chaotic irregularities from the melt pool on the surface due to the gravity slump, or material droop. The directional Ra was also compared with the particle count and showed identical trends to the areal Sa. The maximum height roughness (Rz) is depicted in Fig. 13b and shows similar trends to Ra with the peak of 114 µm, which is the upper limit of the PSD for the powder. The Rz peak height of the upskin surface is constant up to the higher values of the angles, where the powder fills in valley voids and thus Rz decreases.

Prior literature documented that Rz can be approximated by the upper PSD of the powder for L-PBF [74,75]. The experimental data suggest that, for LP-DED, the Rz peak can be approximated by using the maximum PSD. In the downskin surface, there is a decrease in Rz where the surface is shielded from the direct impingement of larger particles. However, the rebounds and recirculation of particles are driven by the smaller and medium-sized particles (ranging from 55 to 95 µm) due to their mass and velocity differences. The 115 µm diameter particle has 83 % larger mass than the 85 µm particle, where the difference between the 55 and 115 µm is 337 %. The velocity in the powder injection has been shown to vary based on mass and surface area of particles as well as nozzle focal plane, thus the likelihood of rebounds and recirculation is higher with the smaller particles. [76,77]. SEM images confirmed that the size of the particles adhered to the downskin 40° and 45° walls is less than 90 µm.

The relationship between waviness and wall thickness is shown in Fig. 14. The waviness is higher on the upskin for most of the angles, although differences are minor at angles below 30°. There is a clear trend of waviness increasing with the wall thickness can be observed and it is due to the surface irregularities from material droop on the downskin. The upskin waviness is driven by the excess material deposition above the nominal melt pool. This results from direct impingement of

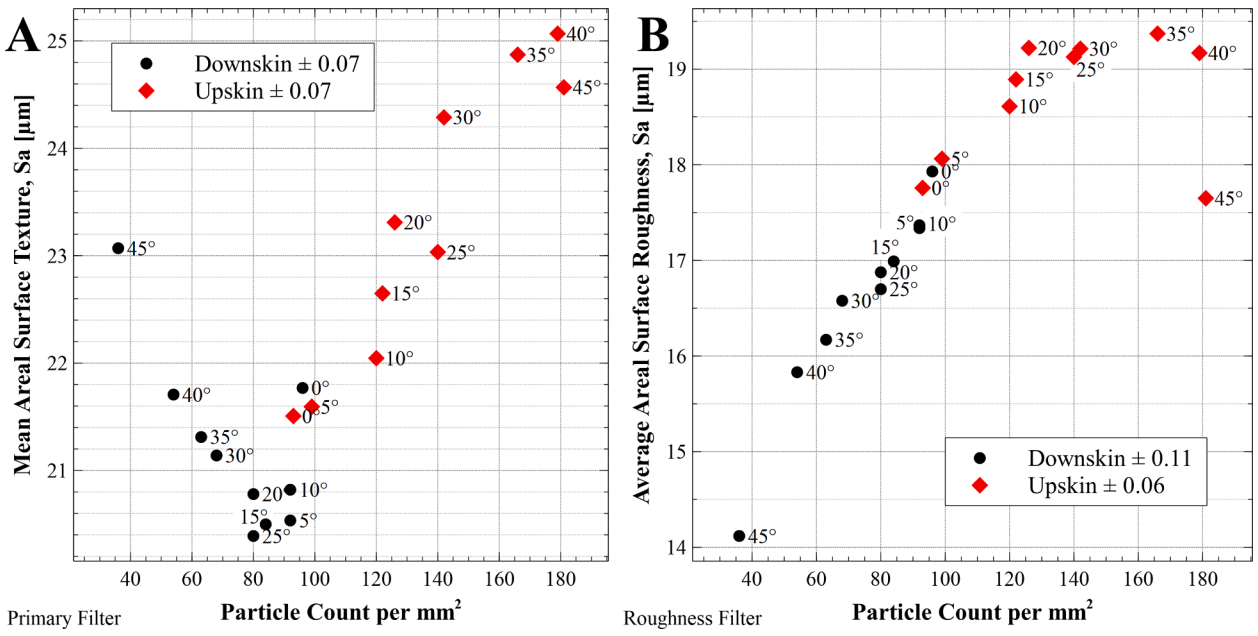

Fig. 12. Roughness compared to particle count from SEM. a) Primary filter and, b) Roughness filter.

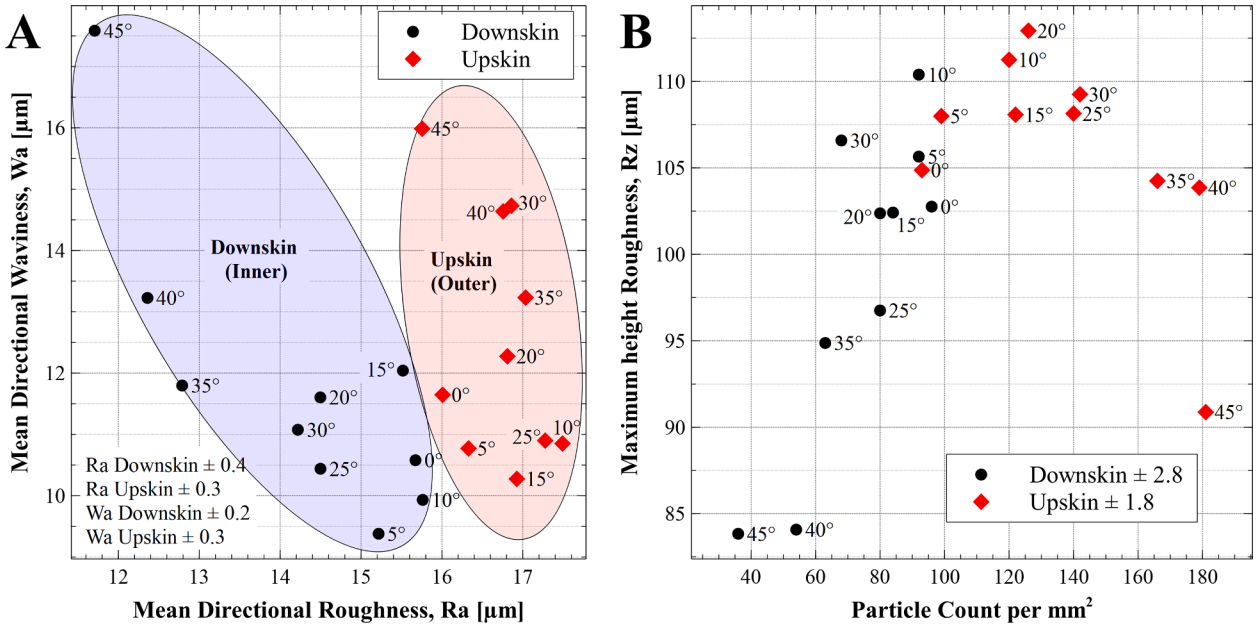

Fig. 13. A) directional vertical roughness and waviness. the shaded blue region indicates the downskin surface and shaded red the upskin surface. b) maximum height (rz) and particle count. (For interpretation of the references to color in this figure legend, the reader is referred to the web version of this article.)

the particles and remelted material flowing upwards and outward breaking the surface tension [78,79]. This phenomenon has been evaluated in single bead LP-DED walls [80], but this study has demonstrated that it is amplified in the angled walls. Prior studies concluded that waviness was caused by the layer thickness [29,81]. This work has proven that the waviness is an order of magnitude lower that Lu et al and Shim et al and uncorrelated to the layer thickness.

4. Conclusions

It was shown that the LP-DED process can produce low porosity (<0.14 %) angled walls with target thickness of 1 mm and with an inclination angle of up to 45° using the NASA HR-1 (Fe-Ni-Cr) alloy. The geometric aspects of the samples including wall thickness, melt pool, and surface texture were evaluated. The surface texture was filtered to properly segment the waviness and roughness parameters to determine their contribution and the causing process mechanisms. From the experimental observations, optical micrographs, SEM images, and optical surface texture measurements, the following conclusions are drawn:

- Walls featuring angles of up to 30° are stable, but angles above that threshold pose higher risks of a build failure. In such cases, it may be necessary to incorporate adjacent wall stiffening to ensure structural integrity.
- The primary areal surface texture (Sa) exhibits an increase with the rise in wall angle, which can be attributed to surface irregularities arising from the melt pool and material droop. Peaks are dominant

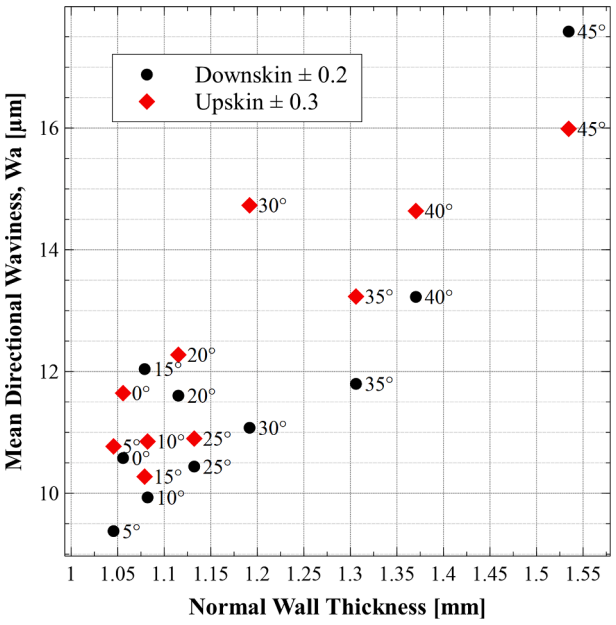

Fig. 14. Directional waviness and normal wall thickness.

for the downskin surface with the increasing angle and reduced for the upskin.

- The waviness and subsequent wall thickness increases with the increased wall angle due to the chaotic surface irregularities from material droop on the downskin. The upskin waviness is driven by the excess material deposition above the nominal melt pool. This is due to direct impingement of the particles and remelted material flowing upwards and outwards.
- Proper filtering of the texture measurements is required to segregate roughness and waviness. Differing conclusions could be drawn about the mechanisms leading to texture if proper filtering is not considered. The λc of 0.8 mm was an appropriate cut-off filter to extract directional roughness and waviness for these thin-wall samples.
- As the angle increases, the filtered average areal and directional surface roughness (Sa, Ra) of the downskin surface significantly decreases. This reduction can be attributed to a decrease in the number of adhered particles on the surface. This trend contradicts the observations documented in the literature regarding surfaces manufactured with the L-PBF process.
- The upskin surface exhibits an increase in average areal (Sa) with an increase in particle count. The roughness crests at 20° and remains constant until the adhered powder filled in voids, resulting in a reduction in roughness at higher build angles.
- The wall thickness increases exponentially with the angle, reaching an inflection point at 30° where the thickness starts to significantly increase due to melt pool droop. A correlation for the estimation of the wall thickness was developed using the data related to the samples made of NASA HR-1 alloy.
- The results obtained from single-pass angled walls indicate that, for LP-DED, the directional maximum profile height (Rz) can be estimated using the maximum particle size distribution. Only particles with size less than 85 µm adhere to the downskin surface at angles above 35° due to higher rebounds and recirculation.
- The stair stepping typically observed in the LP-DED was not detected with a layer height of 0.254 mm and remelting of 4–5 previously deposited layers.

The complex geometry of a part being fabricated inherently alters surface texture due to varied angles. This change is influenced by the build parameters and resulting melt pool. Thickness variation and powder adherence for upskin and downskin follow comparable trends based on wall angle, driven by process mechanisms. Surface texture, encompassing roughness and waviness, varies with alloy, parameters, and resulting LP-DED melt pool. Designers must adhere to geometry guidelines and characterize surface texture, which can impact fatigue life, corrosion, heat transfer, and fluid flow performance. Previous views on LP-DED mandated post-machining, but experiments show properly designed LP-DED can approach L-PBF surface finishes. LP-DED manufacturing holds potential for aerospace, power generation, and industrial heat exchangers.

Declaration of Competing Interest

The authors declare that they have no known competing financial interests or personal relationships that could have appeared to influence the work reported in this paper.

Data availability

Data will be made available on request.

Acknowledgements

This research was funded by NASA under additive manufacturing development efforts through the Rapid Analysis and Manufacturing Propulsion Technology (RAMPT) and Optimized and Repeatable Components using Additive (ORCA) projects. This paper describes objective technical results and analysis. Any subjective views or opinions that might be expressed in the paper do not necessarily represent the views of the National Aeronautics and Space Administration (NASA) or the United States Government. The results from this study are solely for informational purposes and not an endorsement of any techniques by the authors, their employers, or the publishing journal. Thank you to the following individuals that aided with discussions on experiments and data results: Agustin Diaz (REM Surface), RPM Innovations (RPMI), Tyler Blumenthal (RPMI), Sara Rengifo (NASA), and Bhaskar Dutta (DM3D). The authors also acknowledge the use of Veusz software.

Appendix A. Supplementary data

Supplementary data to this article can be found online at https://doi.org/10.1016/j.matdes.2023.112352.

References

[1] P. Gradl, D. Tinker, A. Park, O. Mireles, M. Garcia, R. Wilkerson, C. Mckinney, Robust Metal Additive Manufacturing Process Selection and Development for Aerospace Components, J. Mater. Eng. Performance, Springer (2021), https://doi.org/10.1007/s11665-022-06850-0.

[2] B. Blakey-Milner, P. Gradl, G. Snedden, M. Brooks, J. Pitot, E. Lopez, M. Leary, F. Berto, A. du Plessis, Metal additive manufacturing in aerospace: a review, Mater. Design 209 (2021), 110008, https://doi.org/10.1016/j.matdes.2021.110008.

[3] Z. Wu, S.P. Narra, A. Rollett, Exploring the fabrication limits of thin-wall structures in a laser powder bed fusion process, Int. J. Adv. Manuf. Technol. 110 (2020) 191–207, https://doi.org/10.1007/s00170-020-05827-4.

[4] D. Herzog, K. Asami, C. Scholl, Design guidelines for laser powder bed fusion in Inconel 718, 012015 (2022). 10.2351/7.0000508.

[5] A. Ewald, J. Schlattmann, Design guidelines for laser metal deposition of lightweight structures, LIA Today 26 (2018) 16–19, https://doi.org/10.2351/1.5040612.

[6] S. Gruber, C. Grunert, M. Riede, E. López, A. Marquardt, F. Brueckner, C. Leyens, Comparison of dimensional accuracy and tolerances of powder bed based and nozzle based additive manufacturing processes, J. Laser Appl. 32 (2020), 032016, https://doi.org/10.2351/7.0000115.

[7] P.R. Gradl, D.C. Tinker, J. Ivester, S.W. Skinner, T. Teasley, J.L. Bili, Geometric Feature Reproducibility for Laser Powder Bed Fusion (L-PBF) Additive Manufacturing with Inconel 718, Addit. Manuf. 47 (2021), 102305, https://doi.org/10.1016/j.addma.2021.102305.

[8] J. Berez, M. Praniewicz, C. Saldana, Assessing laser powder bed fusion system geometric errors through artifact-based methods, Procedia Manuf. 53 (2021) 395–406, https://doi.org/10.1016/j.promfg.2021.06.042.

[9] B. Fotovvati, E. Asadi, Size effects on geometrical accuracy for additive manufacturing of Ti-6Al-4V ELI parts, Int. J. Adv. Manuf. Technol. 104 (2019) 2951–2959, https://doi.org/10.1007/s00170-019-04184-1.

[10] S.A. Niknam, M. Mortazavi, D. Li, Additively manufactured heat exchangers: a review on opportunities and challenges, Int. J. Adv. Manuf. Technol. 112 (2021) 601–618, https://doi.org/10.1007/s00170-020-06372-w.

[11] Paul R. Gradl, Omar R. Mireles, Christopher S. Protz, Chance P. Garcia, Metal Additive Manufacturing for Propulsion Applications, 1st ed., American Institute of Aeronautics and Astronautics, Inc., Reston, VA, 2022. https://doi.org/10.2514/4.106279.

[12] F. Kerstens, A. Cervone, P. Gradl, End to end process evaluation for additively manufactured liquid rocket engine thrust chambers, Acta Astronaut. 182 (2021) 454–465, https://doi.org/10.1016/j.actaastro.2021.02.034.

[13] P. Gradl, A. Cervone, P. Colonna, Integral Channel Nozzles and Heat Exchangers using Additive Manufacturing Directed Energy Deposition NASA HR-1 Alloy, in: 73rd Int. Astronaut. Congr., Paris, France, 2022: p. IAC-22,C4,2,x73690.

[14] E. Klein, J. Ling, V. Aute, Y. Hwang, R. Radermacher, A Review of Recent Advances in Additively Manufactured Heat Exchangers, Int. Refrig. Air Cond. Conf. (2018) 1–10. https://docs.lib.purdue.edu/iracc%0Ahttps://docs.lib.purdue.edu/iracc/1983.

[15] E. Handler, A. Sterling, J. Pegues, H. Ozdes, M. Masoomi, N. Shamsaei, S. Thompson, Design and Process Considerations for Effective Additive Manufacturing of Heat Exchangers, 2019. https://sffsymposium.engr.utexas.edu/sites/default/files/2017/Manuscripts/DesignandProcessConsiderationsforEffectiveAd.pdf.

[16] F. Ascione, A. Conrozier, A. Sakly, P. Planquart, J.M. Hugo, D. Laboureur, Aerothermal Characterization of a Compact Heat Exchanger Element By Additive Manufacturing, Aerospace Europe Conf (2020).

[17] M. Alsulami, M. Mortazavi, S.A. Niknam, D. Li, Design complexity and performance analysis in additively manufactured heat exchangers, Int. J. Adv. Manuf. Technol. 110 (2020) 865–873, https://doi.org/10.1007/s00170-020-05898-3.

[18] X. Zhang, H. Keramati, M. Arie, F. Singer, R. Tiwari, A. Shooshtari, M. Ohadi, Recent Developments in High Temperature Heat Exchangers: A Review, Front, Heat Mass Transf. 11 (2018) 11–18, https://doi.org/10.5098/hmt.11.18.

[19] A. Dass, A. Moridi, State of the Art in Directed Energy Deposition: From Additive Manufacturing to Materials Design, Coatings 9 (2019) 418, https://doi.org/10.3390/coatings9070418.

[20] D.G. Ahn, Directed Energy Deposition (DED) Process: State of the Art, Int. J. of Precis. Eng. and Manuf.-Green Tech. 8 (2) (2021) 703–742, https://doi.org/10.1007/s40684-020-00302-7.

[21] P.R. Gradl, C.S. Protz, Technology advancements for channel wall nozzle manufacturing in liquid rocket engines, Acta Astronaut. 174 (2020), https://doi.org/10.1016/j.actaastro.2020.04.067.

[22] P.R. Gradl, C. Protz, T. Wammen, Additive manufacturing development and hot-fire testing of liquid rocket channel wall nozzles using blown powder directed energy deposition inconel 625 and jbk-75 alloys, in: AIAA Propuls. Energy Forum Expo. 2019, American Institute of Aeronautics and Astronautics Inc, AIAA, 2019. 10.2514/6.2019-4362.

[23] P.R. Gradl, T.W. Teasley, C.S. Protz, C. Katsarelis, P. Chen, Process Development and Hot-fire Testing of Additively Manufactured NASA HR-1 for Liquid Rocket Engine Applications, in: AIAA Propuls. Energy 2021, 2021: pp. 1–23. 10.2514/6.2021-3236.

[24] S. Imbrogno, A. Alhuzaim, M.M. Attallah, Influence of the laser source pulsing frequency on the direct laser deposited Inconel 718 thin walls, J. Alloy. Compd. 856 (2021), 158095, https://doi.org/10.1016/j.jallcom.2020.158095.

[25] M.-N. Bold, J. Zielinski, S. Ziegler, Johannes Henrich Schleifenbaum, Study of laser metal deposition of IN718 on inclined planes: influences of inclination on height and width of deposited material, in: Met. Addit. Manuf. Conf., Orebro, Sweden, 2020.

[26] P. Xue, L. Zhu, P. Xu, Y. Ren, B. Xin, S. Wang, Z. Yang, J. Ning, G. Meng, Z. Liu, CrCoNi medium-entropy alloy thin-walled parts manufactured by laser metal deposition: Microstructure evolution and mechanical anisotropy, Mater. Sci. Eng. A 817 (2021), 141306, https://doi.org/10.1016/j.msea.2021.141306.

[27] R. Jardin, V. Tuninetti, J. Tchuindjang, N. Hashemi, R. Carrus, A. Mertens, L. Duch, H.S. Tran, A.M. Habraken, Sensitivity analysis in the modelling of a high speed steel thin-wall produced by directed energy deposition, Metals (basel) 10 (2020) 1554, https://doi.org/10.3390/met10111554.

[28] J. Zhang, S. Shi, G. Fu, J. Shi, G. Zhu, D. Cheng, Analysis on surface finish of thin-wall parts by laser metal deposition with annular beam, Opt. Laser Technol. 119 (2019), 105605, https://doi.org/10.1016/j.optlastec.2019.105605.

[29] L. Lu, T. Shi, J. Zhang, Y. Mei, D. Cheng, G. Fu, S. Yu, Research on surface finish of thin-wall parts by laser with coaxial inside-beam powder feeding, J. Laser Appl. 33 (2021), 022003, https://doi.org/10.2351/7.0000206.

[30] G. Zhu, D. Li, A. Zhang, G. Pi, Y. Tang, The influence of laser and powder defocusing characteristics on the surface quality in laser direct metal deposition, Opt. Laser Technol. 44 (2012) 349–356, https://doi.org/10.1016/j.optlastec.2011.07.013.

[31] D. Svetlizky, B. Zheng, A. Vyatskikh, M. Das, S. Bose, A. Bandyopadhyay, J. M. Schoenung, E.J. Lavernia, N. Eliaz, Laser-based directed energy deposition (DED-LB) of advanced materials, Mater. Sci. Eng. A 840 (2022), 142967, https://doi.org/10.1016/j.msea.2022.142967.

[32] X. Wang, Z. Liu, Z. Guo, Y. Hu, A fundamental investigation on three–dimensional laser material deposition of AISI316L stainless steel, Opt. Laser Technol. 126 (2020), 106107, https://doi.org/10.1016/j.optlastec.2020.106107.

[33] J.C. Pereira, H. Borovkov, F. Zubiri, M.C. Guerra, J. Caminos, Optimization of Thin Walls with Sharp Corners in SS316L and IN718 Alloys Manufactured with Laser Metal Deposition, J. Manuf. Mater. Process. 5 (2021) 5, https://doi.org/10.3390/jmmp5010005.

[34] A. Komodromos, F. Kolpak, A.E. Tekkaya, Manufacturing of Integrated Cooling Channels by Directed Energy Deposition for Hot Stamping Tools with Ball Burnished SurfacesHerstellung von integrierten Kühlkanälen durch Laserpulverauftragsschweißen für Presshärtewerkzeuge mit glattgewalzten Oberflächen, BHM Berg- Huettenmaenn. Monatsh. 167 (9) (2022) 428–434.

[35] A.C. Paul, A.N. Jinoop, C.P. Paul, P. Deogiri, K.S. Bindra, Investigating build geometry characteristics during laser directed energy deposition based additive manufacturing, J. Laser Appl. 32 (2020), 042002, https://doi.org/10.2351/7.0000004.

[36] M. Urbánek, J. Hodek, D. Melzer, M. Koukolíková, A. Prantl, J. Vavřík, M. Brázda, P. Martínek, S. Rzepa, J. Džugan, Prediction of Behaviour of Thin-Walled DED-Processed Structure: Experimental-Numerical Approach, Materials 15 (2022) 806, https://doi.org/10.3390/ma15030806.

[37] M. Gharbi, P. Peyre, C. Gorny, M. Carin, S. Morville, P. Le Masson, D. Carron, R. Fabbro, Influence of various process conditions on surface finishes induced by the direct metal deposition laser technique on a Ti-6Al-4V alloy, J. Mater. Process. Technol. 213 (2013) 791–800, https://doi.org/10.1016/j.jmatprotec.2012.11.015.

[38] H. Kalami, J. Urbanic, Process planning solution strategies for fabrication of thin-wall domes using directed energy deposition, Int. J. Comput. Integr. Manuf. 00 (2021) 1–17, https://doi.org/10.1080/0951192X.2021.1946851.

[39] H. Kalami, J. Urbanic, Exploration of surface roughness measurement solutions for additive manufactured components built by multi-axis tool paths, Addit. Manuf. 38 (2021), 101822, https://doi.org/10.1016/j.addma.2020.101822.

[40] F. Kaji, A.N. Jinoop, M. Zimny, G. Frikel, K. Tam, E. Toyserkani, Process Planning for Additive Manufacturing of Geometries with Variable Overhang Angles using a Robotic Laser Directed Energy Deposition system, Addit. Manuf. Lett. 2 (2022), 100035, https://doi.org/10.1016/j.addlet.2022.100035.

[41] X. Wang, D. Deng, Y. Hu, F. Ning, H. Wang, W. Cong, H. Zhang, Overhang structure and accuracy in laser engineered net shaping of Fe-Cr steel, Opt. Laser Technol. 106 (2018) 357–365, https://doi.org/10.1016/j.optlastec.2018.04.015.

[42] D. Rosen, S. Kim, Design and Manufacturing Implications of Additive Manufacturing, J. Mater. Eng. Perform. (2021), https://doi.org/10.1007/s11665-021-06030-6.

[43] J. Boban, A. Ahmed, Improving the surface integrity and mechanical properties of additive manufactured stainless steel components by wire electrical discharge polishing, J. Mater. Process. Technol. 291 (2021), 117013, https://doi.org/10.1016/j.jmatprotec.2020.117013.

[44] M.A. Melia, J.G. Duran, J.R. Koepke, D.J. Saiz, B.H. Jared, E.J. Schindelholz, How build angle and post-processing impact roughness and corrosion of additively manufactured 316L stainless steel, npj Mater. Degrad. 4 (2020) 1–11, https://doi.org/10.1038/s41529-020-00126-5.

[45] A. Diaz, Surface texture characterization and optimization of metal additive manufacturing-produced components for aerospace applications, Addit. Manuf. Aerosp. Ind. (2019) 341–374, https://doi.org/10.1016/B978-0-12-814062-8.00018-2.

[46] A.J. Brooks, A. Dhakad, A. Diaz, D. Kowalik, Toward Understanding the Role of Surface Texture for Additively Manufactured Metal Parts, Struct. Integr. Addit. Manuf. Mater. Parts. ASTM Inter (2020) 61–87, https://doi.org/10.1520/stp163120190160.

[47] P. Pawlus, R. Reizer, M. Wieczorowski, Functional importance of surface texture parameters, Materials (basel). 14 (2021) 1–29, https://doi.org/10.3390/ma14185326.

[48] T. DebRoy, H.L. Wei, J.S. Zuback, T. Mukherjee, J.W. Elmer, J.O. Milewski, A. M. Beese, A. Wilson-Heid, A. De, W. Zhang, Additive manufacturing of metallic components – Process, structure and properties, Prog. Mater Sci. 92 (2018) 112–224, https://doi.org/10.1016/j.pmatsci.2017.10.001.

[49] D. Obilanade, C. Dordlofva, P. Törlind, Surface roughness considerations in design for additive manufacturing - A literature review, Proc. Des. Soc. 1 (2021) 2841–2850, https://doi.org/10.1017/pds.2021.545.

[50] S. Murchio, M. Dallago, F. Zanini, S. Carmignato, G. Zappini, F. Berto, D. Maniglio, M. Benedetti, Additively manufactured Ti–6Al–4V thin struts via laser powder bed fusion: Effect of building orientation on geometrical accuracy and mechanical properties, J. Mech. Behav. Biomed. Mater. 119 (2021), 104495, https://doi.org/10.1016/j.jmbbm.2021.104495.

[51] J.C. Fox, S.P. Moylan, B.M. Lane, Effect of Process Parameters on the Surface Roughness of Overhanging Structures in Laser Powder Bed Fusion Additive Manufacturing, Procedia CIRP. 45 (2016) 131–134, https://doi.org/10.1016/j.procir.2016.02.347.

[52] Y. Tian, D. Tomus, P. Rometsch, X. Wu, Influences of processing parameters on surface roughness of Hastelloy X produced by selective laser melting, Addit. Manuf. 13 (2017) 103–112, https://doi.org/10.1016/j.addma.2016.10.010.

[53] J.C. Snyder, K.A. Thole, Understanding Laser Powder Bed Fusion Surface Roughness, J. Manuf. Sci. Eng. 142 (2020), https://doi.org/10.1115/1.4046504.

[54] A. Charles, A. Elkaseer, U. Paggi, L. Thijs, V. Hagenmeyer, S. Scholz, Down-facing surfaces in laser powder bed fusion of Ti6Al4V: Effect of dross formation on dimensional accuracy and surface texture, Addit. Manuf. 46 (2021), 102148, https://doi.org/10.1016/J.ADDMA.2021.102148.

[55] O. Abdulhameed, A. Al-Ahmari, W. Ameen, S.H. Mian, Additive manufacturing: Challenges, trends, and applications, Adv. Mech. Eng. 11 (2019) 168781401882288. 10.1177/1687814018822880.

[56] A.N. Jinoop, C.P. Paul, S.K. Mishra, K.S. Bindra, Laser Additive Manufacturing using directed energy deposition of Inconel-718 wall structures with tailored

characteristics, Vacuum 166 (2019) 270–278, https://doi.org/10.1016/j.vacuum.2019.05.027.
[57] N. Shamsaei, A. Yadollahi, L. Bian, S.M. Thompson, An overview of Direct Laser Deposition for additive manufacturing; Part II: Mechanical behavior, process parameter optimization and control, Addit. Manuf. 8 (2015) 12–35, https://doi.org/10.1016/j.addma.2015.07.002.
[58] P. Stavropoulos, P. Foteinopoulos, Modelling of additive manufacturing processes: a review and classification, Manuf. Rev. 5 (2018) 2, https://doi.org/10.1051/mfreview/2017014.
[59] P.R. Gradl, A. Cervone, E. Gill, Surface texture characterization for thin-wall NASA HR-1 Fe – Ni – Cr alloy using laser powder directed energy deposition (LP-DED), Adv. Ind. Manuf. Eng. 4 (2022), 100084, https://doi.org/10.1016/j.aime.2022.100084.
[60] A. Soltani-tehrani, P. Chen, C. Katsarelis, P. Gradl, S. Shao, Thin-Walled Structures Mechanical properties of laser powder directed energy deposited NASA HR-1 superalloy : Effects of powder reuse and part orientation, Thin-Walled Struct. 185 (2023), 110636, https://doi.org/10.1016/j.tws.2023.110636.
[61] A. Soltani-tehrani, P. Chen, C. Katsarelis, P. Gradl, S. Shao, N. Shamsaei, Laser powder directed energy deposition (LP-DED) NASA HR-1 alloy : Laser power and heat treatment effects on microstructure and mechanical properties, Addit. Manuf. Lett. 3 (2022), 100097, https://doi.org/10.1016/j.addlet.2022.100097.
[62] P. Gradl, O.R. Mireles, C. Katsarelis, T.M. Smith, J. Sowards, A. Park, P. Chen, D. C. Tinker, C. Protz, T. Teasley, D.L. Ellis, C. Kantzos, Advancement of Extreme Environment Additively Manufactured Alloys for Next Generation Space Propulsion Applications, Acta Astronaut. 211 (2023) 483–497.
[63] F. Marinello, A. Pezzuolo, Application of ISO 25178 standard for multiscale 3D parametric assessment of surface topographies, IOP Conf. Ser. Earth Environ. Sci. 275 (2019), https://doi.org/10.1088/1755-1315/275/1/012011.
[64] ISO, ISO 13565-2:1996: Geometrical Product Specifications (GPS) — Surface texture: Profile method; Surfaces having stratified functional properties — Part 2: Height characterization using the linear material ratio curve, 1996. https://www.iso.org/standard/22280.html.
[65] American Society of Mechanical Engineers (ASME), Surface texture : surface roughness, waviness, and lay : ASME B46.1-2019, New York, N.Y, 2019. https://www.asme.org/codes-standards/find-codes-standards/b46-1-surface-texture (accessed December 29, 2021).
[66] International Organization for Standardization, ISO 25178-2 Geometrical product specifications (GPS) — Surface texture: Areal — Part 2: Terms, definitions and surface texture parameters, Geneva, 2021. https://www.iso.org/standard/74591.html.
[67] J.C. Haley, J.M. Schoenung, E.J. Lavernia, Modelling particle impact on the melt pool and wettability effects in laser directed energy deposition additive manufacturing, Mater. Sci. Eng. A 761 (2019), https://doi.org/10.1016/j.msea.2019.138052.
[68] M. Mazzarisi, S.L. Campanelli, A. Angelastro, M. Dassisti, Phenomenological modelling of direct laser metal deposition for single tracks, Int. J. Adv. Manuf. Technol. 111 (2020) 1955–1970, https://doi.org/10.1007/s00170-020-06204-x.
[69] F. Wirth, S. Arpagaus, K. Wegener, Analysis of melt pool dynamics in laser cladding and direct metal deposition by automated high-speed camera image evaluation, Addit. Manuf. 21 (2018) 369–382, https://doi.org/10.1016/J.ADDMA.2018.03.025.
[70] B. Song, T. Yu, X. Jiang, W. Xi, X. Lin, Z. Ma, Z. Wang, Development of the molten pool and solidification characterization in single bead multilayer direct energy deposition, Addit. Manuf. 49 (2022), 102479, https://doi.org/10.1016/j.addma.2021.102479.
[71] B. Rosa, A. Brient, S. Samper, J.-y. Hascoët, Operating parameters and multi-scale topography modeling of additive laser manufacturing process, 5th Int, Conf. Surf. Metrol. 4th. 4 (2016) 1–9, https://doi.org/10.1088/2051-672X/4/4/045002.
[72] K. Shah, A.J. Pinkerton, A. Salman, L. Li, Effects of melt pool variables and process parameters in laser direct metal deposition of aerospace alloys, Mater. Manuf. Process. 25 (2010) 1372–1380, https://doi.org/10.1080/10426914.2010.480999.
[73] A. Azarniya, X.G. Colera, M.J. Mirzaali, S. Sovizi, F. Bartolomeu, M. k. St Weglowski, W.W. Wits, C.Y. Yap, J. Ahn, G. Miranda, F.S. Silva, H.R. Madaah Hosseini, S. Ramakrishna, A.A. Zadpoor, M. St Weglowski k, W.W. Wits, C.Y. Yap, J. Ahn, G. Miranda, F.S. Silva, H.R. Madaah Hosseini, S. Ramakrishna, A.A. Zadpoor, Additive manufacturing of Ti–6Al–4V parts through laser metal deposition (LMD): Process, microstructure, and mechanical properties, J. Alloys Compd. 804 (2019) 163–191. 10.1016/j.jallcom.2019.04.255.
[74] J.Y. Lee, A.P. Nagalingam, S.H. Yeo, A review on the state-of-the-art of surface finishing processes and related ISO/ASTM standards for metal additive manufactured components, Virtual Phys. Prototyp. (2020) 1–29, https://doi.org/10.1080/17452759.2020.1830346.
[75] M. Heinl, M. Heinl, S. Greiner, K. Wudy, C. Pobel, M. Rasch, M. Rasch, F. Huber, F. Huber, T. Papke, M. Merklein, M. Schmidt, M. Schmidt, C. Körner, D. Drummer, T. Hausotte, Measuring procedures for surface evaluation of additively manufactured powder bed-based polymer and metal parts, Meas. Sci. Technol. 31 (2020), https://doi.org/10.1088/1361-6501/ab89e2.
[76] A.D. Iams, M.Z. Gao, A. Shetty, T.A. Palmer, Influence of particle size on powder rheology and effects on mass flow during directed energy deposition additive manufacturing, Powder Technol. 396 (2021) 316–326, https://doi.org/10.1016/j.powtec.2021.10.059.
[77] G. Piscopo, E. Atzeni, A. Saboori, An Overview of the Process Mechanisms in the Laser Powder Directed Energy Deposition, Appl. Sci. 13 (2023) 117, https://doi.org/10.3390/app13010117.
[78] L. Han, F.W. Liou, K.M. Phatak, Modeling of laser cladding with powder injection, Metall. Mater. Trans. B 35 (2004) 1139–1150, https://doi.org/10.1007/s11663-004-0070-0.
[79] Z. Li, G. Yu, X. He, S. Li, Z. Shu, Surface Tension-Driven Flow and Its Correlation with Mass Transfer during L-DED of Co-Based Powders, Metals (basel). 12 (2022), https://doi.org/10.3390/met12050842.
[80] Y.S. Lee, D.F. Farson, Surface tension-powered build dimension control in laser additive manufacturing process, Int. J. Adv. Manuf. Technol. 85 (2015) 1035–1044, https://doi.org/10.1007/s00170-015-7974-5.
[81] D.S. Shim, G.Y. Baek, J.S. Seo, G.Y. Shin, K.P. Kim, K.Y. Lee, Effect of layer thickness setting on deposition characteristics in direct energy deposition (DED) process, Opt. Laser Technol. 86 (2016) 69–78, https://doi.org/10.1016/j.optlastec.2016.07.001.